LETTER

https://doi.org/10.1038/s41586-019-1052-3

Van der Waals contacts between three-dimensional metals and two-dimensional semiconductors

Yan Wang[1,2], Jong Chan Kim[3], Ryan J. Wu[4], Jenny Martinez[5], Xiuju Song[2,6], Jieun Yang[1,2], Fang Zhao[7], Andre Mkhoyan[4], Hu Young Jeong[3] & Manish Chhowalla[1,2,6]*

As the dimensions of the semiconducting channels in field-effect transistors decrease, the contact resistance of the metal–semiconductor interface at the source and drain electrodes increases, dominating the performance of devices[1–3]. Two-dimensional (2D) transition-metal dichalcogenides such as molybdenum disulfide (MoS_2) have been demonstrated to be excellent semiconductors for ultrathin field-effect transistors[4,5]. However, unusually high contact resistance has been observed across the interface between the metal and the 2D transition-metal dichalcogenide[3,5–9]. Recent studies have shown that van der Waals contacts formed by transferred graphene[10,11] and metals[12] on few-layered transition-metal dichalcogenides produce good contact properties. However, van der Waals contacts between a three-dimensional metal and a monolayer 2D transition-metal dichalcogenide have yet to be demonstrated. Here we report the realization of ultraclean van der Waals contacts between 10-nanometre-thick indium metal capped with 100-nanometre-thick gold electrodes and monolayer MoS_2. Using scanning transmission electron microscopy imaging, we show that the indium and gold layers form a solid solution after annealing at 200 degrees Celsius and that the interface between the gold-capped indium and the MoS_2 is atomically sharp with no detectable chemical interaction between the metal and the 2D transition-metal dichalcogenide, suggesting van-der-Waals-type bonding between the gold-capped indium and monolayer MoS_2. The contact resistance of the indium/gold electrodes is 3,000 ± 300 ohm micrometres for monolayer MoS_2 and 800 ± 200 ohm micrometres for few-layered MoS_2. These values are among the lowest observed for three-dimensional metal electrodes evaporated onto MoS_2, enabling high-performance field-effect transistors with a mobility of 167 ± 20 square centimetres per volt per second. We also demonstrate a low contact resistance of 220 ± 50 ohm micrometres on ultrathin niobium disulfide (NbS_2) and near-ideal band offsets, indicative of defect-free interfaces, in tungsten disulfide (WS_2) and tungsten diselenide (WSe_2) contacted with indium alloy. Our work provides a simple method of making ultraclean van der Waals contacts using standard laboratory technology on monolayer 2D semiconductors.

Field-effect transistors (FETs) using 2D semiconductors as the channel material offer excellent gate electrostatics, which allows mitigation of short channel effects—making them interesting for sub-10-nm node devices[13]. However, in short-channel devices, the transport through the semiconductor is nearly ballistic and almost all of the power is dissipated at the contacts[1]. Thus, optimizing the contacts between 2D semiconductors and metal electrodes is an important technological challenge. Several strategies, such as phase engineering to create lateral metal–semiconductor–metal heterojunctions[14], formation of clean interfaces via van der Waals contacts using graphene[10,11], mechanical transfer of metal films[12] and using hexagonal boron nitride (h-BN) as the tunnel barrier[15], have been reported to improve the electrical properties of contacts on 2D materials. The main challenge in making contacts on atomically thin materials exposed to the atmosphere is the presence of adsorbed water or hydrocarbon layers on their surface. The thickness of these layers is comparable to that of 2D semiconductors so that when metal electrodes are deposited, the adsorbed contaminants are incorporated at the interface between the metal and the 2D semiconductor. This leads to the creation of interface states that can pin the Fermi level and increase the contact resistance[16]. It is possible to minimize the impact of adsorbed layers by depositing metal electrodes under ultrahigh vacuum[17,18], which reduces the contact resistance. In addition, the transfer of thin metal films[12] or few-layered mechanically exfoliated h-BN[15] on top of 2D semiconductors can squeeze out adsorbed layers. However, even when the adsorbed layer is removed, the direct deposition of metal can lead to substantial damage via kinetic energy transfer or chemical reaction between the metal atoms and the 2D semiconductor. Studies have shown that creation of van der Waals contacts via metal transfer[12], graphene[10,11] or h-BN[15] on 2D semiconductors can create clean interfaces without damaging the underlying 2D semiconductor. However, all of these strategies for improving contact properties have been reported for multi-layer 2D semiconductors; clean interfaces with low contact resistance have yet to be reported for single layers.

We have characterized the ultraclean van der Waals interface formed between monolayer 2D MoS_2 and indium/gold (In/Au) electrodes deposited using a standard laboratory electron-beam evaporator under normal vacuum ($<10^{-6}$ Torr) using annular dark field (ADF) scanning transmission electron microscopy (STEM) and X-ray photoelectron spectroscopy (XPS). The electrodes consist of 10-nm-thick In capped with 100-nm-thick Au to prevent reaction of In with the environment. The schematic of the FET device tested in this work is shown in Fig. 1a (see Methods for details of electrode deposition and device fabrication). To image and study the interface between In/Au and MoS_2, we conducted cross-sectional ADF STEM. It is well known that monolayer and few-layered transition-metal dichalcogenides are damaged during metal deposition[12,16] and that only dry transfer of electrodes provide clean and intact interfaces[12]. By contrast, our analysis reveals that the In/Au–MoS_2 interfaces for monolayer (see Fig. 1b, a broader view image is provided in Extended Data Fig. 1a) and few-layered (see Extended Data Fig. 1b, d) MoS_2 are atomically sharp with no detectable evidence of reaction between the layers of In/Au and MoS_2. The ADF and bright-field STEM images in Fig. 1b clearly show the monolayer MoS_2 and In/Au alloy contact on top with atomic resolution. An ADF intensity profile across the interface for In/Au on monolayer MoS_2 revealed that the spacing between the sulfur atoms and In/Au atoms is 2.4 Å ± 0.3 Å (Extended Data Fig. 1c)—indicating that the In gently deposits on the 2D semiconductor without causing any damage. Our chemical analysis reveals that only vacuum in the form of a van der Waals gap is observed at the interface and that no evidence for oxidation or indium sulfide formation is observed. XPS was performed

[1]Department of Materials Science and Metallurgy, University of Cambridge, Cambridge, UK. [2]Materials Science and Engineering, Rutgers University, Piscataway, NJ, USA. [3]UNIST Central Research Facilities (UCRF) and School of Materials Science and Engineering, UNIST, Ulsan, South Korea. [4]Department of Chemical Engineering and Material Science, University of Minnesota, Minneapolis, MN, USA. [5]Mechanical Engineering, California State Polytechnic University, Pomona, Pomona, CA, USA. [6]International Collaborative Laboratory of 2D Materials for Optoelectronics Science and Technology, Shenzhen University, Shenzhen, China. [7]Department of Physics, Princeton University, Princeton, NJ, USA. *e-mail: mc209@cam.ac.uk

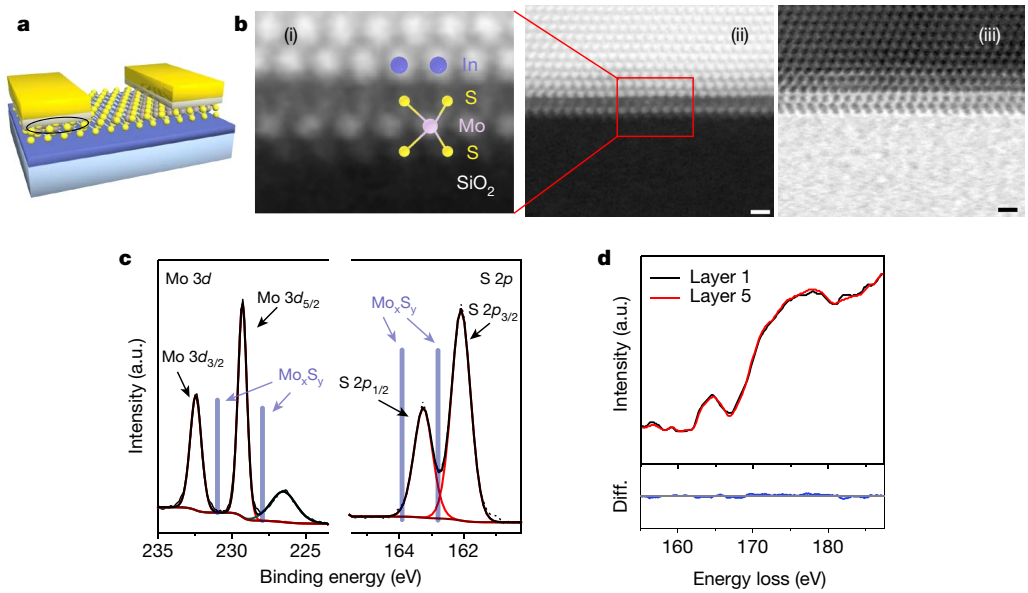

Fig. 1 | Atomic resolution imaging and chemical analyses of In/Au-MoS_2 interface. a, Device structure of the bottom-gate FET used in this study. The electrodes consist of 10-nm-thick In capped with 100-nm-thick Au. The ellipse under the contact indicates the interface region that was analysed using high-resolution STEM. **b**, Atomic-resolution images of In/Au on monolayer MoS_2. (ii), Low-pass filtered ADF STEM image showing Mo, S and In/Au atoms as indicated by the enlarged image (i). (iii), Corresponding bright-field STEM image of the monolayer. Scale bars, 5 Å. **c**, XPS of the In/Au–MoS_2 interface showing pristine Mo and S peaks. The XPS also shows that the deposition of In/Au does not modify the MoS_2. **d**, Electron energy loss spectroscopy of the S $L_{2,3}$-edge, showing that the sulfur atoms of the top layer are completely unaffected by the deposition of metal on top. The sulfur peaks of the topmost and the fifth layer are the same within the precision of the measurement, as indicated by the difference spectra (Diff.) shown in the bottom panel. a.u., arbitrary units.

to characterize the chemistry at the interface between the uppermost sulfur layer and the In/Au alloy. The binding energy values for the Mo 3*d* and S 2*p* doublets were found to be 229.3 eV (Mo $3d_{5/2}$) and 162.1 eV (S $2p_{3/2}$)—typical of pristine MoS_2 (ref. [19]). Nonstoichiometric Mo_xS_y peaks were not observed, as indicated in Fig. 1c. Additional information about the chemical state of the interface is provided by the In 3*d* spectra and In MNN Auger measurements in Extended Data Fig. 1e, f. We corroborated this using electron energy loss spectroscopy (Fig. 1d). The electron energy loss spectroscopy was measured using a focused electron beam probe with spatial resolution of 0.8 Å so that the spectra from highly localized regions at the interface could be obtained. It can be seen that the sulfur $L_{2,3}$-edge exhibits an experimentally negligible difference between the topmost MoS_2 layer in contact with the In/Au and the fifth layer of MoS_2—suggesting that the deposition of In and Au does not introduce any chemical reactions, distortions or strain at the metal/semiconductor interface or within the 2D MoS_2.

To investigate whether the excellent structural features of van der Waals contacts with In/Au can be translated into better device performance, we measured the contact resistance using the transmission line method (TLM) and also the FET properties. The TLM results shown in Fig. 2a for In/Au electrodes on chemical vapour deposition (CVD)-grown monolayer MoS_2 (see Extended Data Fig. 1g, h) reveal a contact resistance of 3.3 ± 0.3 kΩ μm (at $n = 5.0 \times 10^{12}$ cm^{-2}) and values of 800 ± 200 Ω μm (at $n = 3.1 \times 10^{12}$ cm^{-2}, Extended Data Fig. 2a) were measured for few-layered mechanically exfoliated MoS_2. The higher contact resistance in monolayer MoS_2 compared to the few-layered material can be attributed to substrate-carrier scattering[17]. Despite this, the contact resistances of In/Au electrodes on monolayer MoS_2 (Fig. 2b, c)

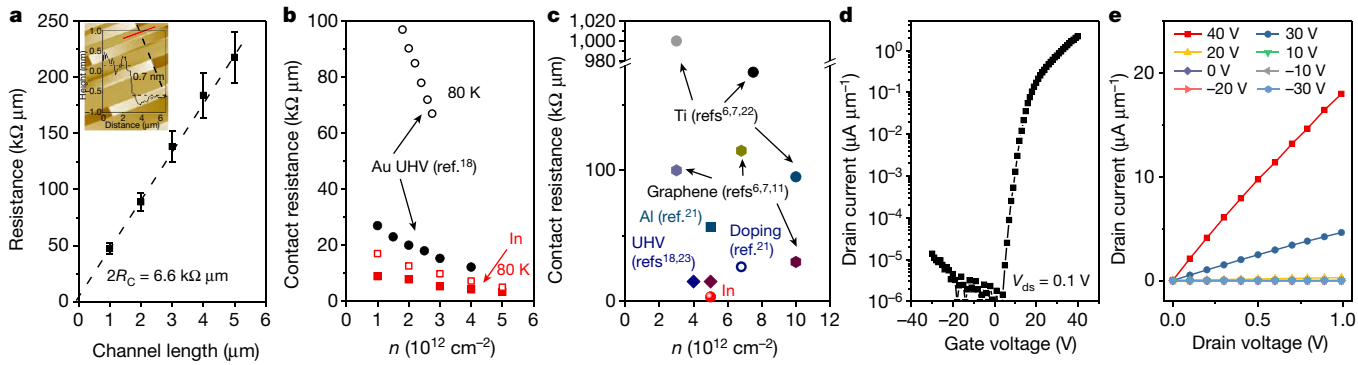

Fig. 2 | Contact resistance and device properties of In/Au electrodes on monolayer MoS_2. a, Contact resistance R_C extracted using TLM. The error bars result from the averaging of least five measurements; this is the same for all the TLM results mentioned in this work. **b**, Contact resistance versus carrier concentration *n* for In/Au electrodes at room temperature (filled points) and at 80 K (open points). Au electrodes deposited under ultrahigh vacuum (UHV, 10^{-9} Torr) are provided for comparison[18]. **c**, Comparison of contact resistance from the literature and our results for different types of electrode materials[6,7,11,18,21–23]. **d**, Typical transfer characteristics of a field-effect transistor with monolayer MoS_2 as the channel and In/Au alloy as the source and drain electrodes. The length and width of the device are 2 μm and 6 μm. A mobility of about 170 cm^2 V^{-1} s^{-1} can be achieved with In/Au electrodes. **e**, Linear output characteristics indicating the absence of a contact barrier.

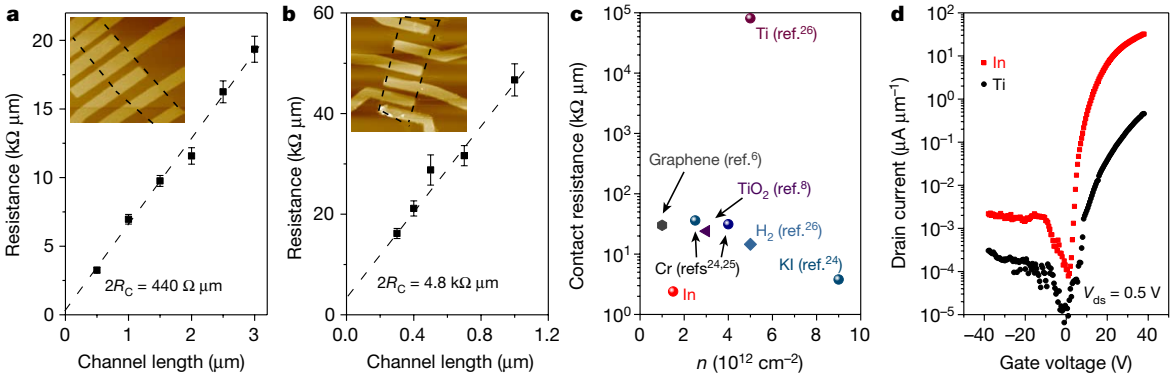

Fig. 3 | Contact properties of In/Au electrodes on 2D NbS_2 and WS_2. **a**, TLM contact resistance of In/Au electrodes on CVD-grown NbS_2. **b**, TLM contact resistance of In/Au electrodes on mechanical exfoliated WS_2. **c**, Contact resistance versus carrier concentration from different studies reported in the literature[6,8,24–26]. It can be seen that the In/Au electrodes exhibit the lowest values. **d**, Transfer characteristics of FETs with WS_2 as the channel material and In/Au contacts; the length and width of the device are 1 μm and 1.2 μm at drain voltage $V_{ds} = 0.5$ V. The transfer curve of Ti-contacted WS_2 device is included for comparison; length and width of the devices are 0.5 μm and 2 μm. In/Au devices show substantially better mobility (approximately 85 cm^2 V^{-1} s^{-1}) than do devices with Ti electrodes (approximately 1 cm^2 V^{-1} s^{-1}).

and few-layered MoS_2 (Extended Data Fig. 2b, c) are among the lowest reported in the literature (Extended Data Table 1) so far at all the carrier concentrations that we measured and at low temperature. For comparison, pure Au electrodes deposited under ultrahigh vacuum have slightly higher contact resistance than In/Au devices (Fig. 2b, c) and the contact resistance of graphene side contacts on h-BN-encapsulated few-layered MoS_2 at 100 K has been measured to be 1,200 Ω μm (at $n = 6.85 \times 10^{12}$ cm^{-2})[15].

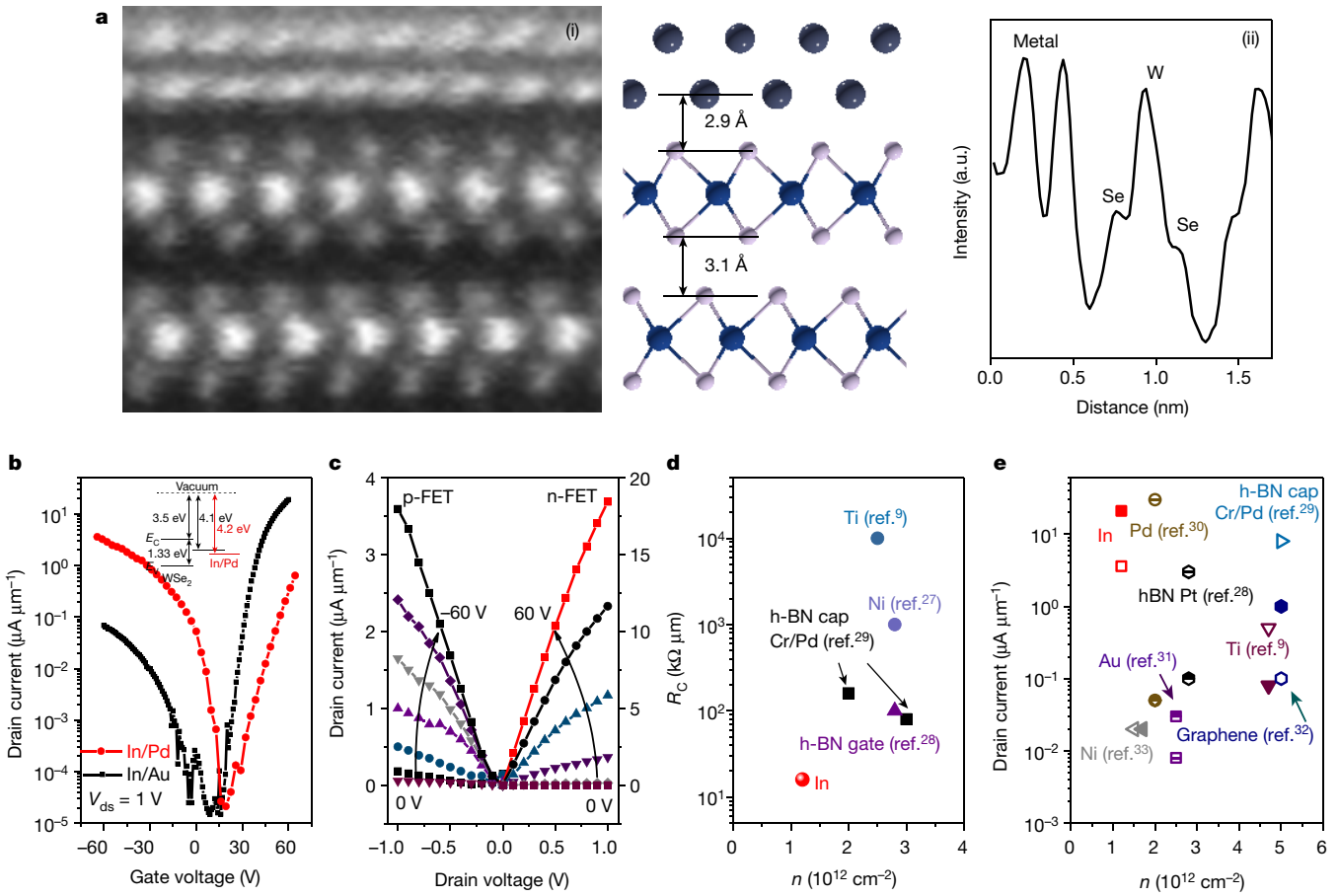

Fig. 4 | In alloy contacts on ultrathin WSe_2. **a**, Atomic-resolution ADF STEM image and corresponding schematic of the In/Au–WSe_2 interface, showing a clear van der Waals gap corresponding to spacing between the Se and In/Au metal atoms. (ii), Intensity profile of (i) showing that the distance between the bottom metal and top selenium is 2.9 Å. **b**, Ambipolar transfer characteristics showing n-type-dominant behaviour with In/Au contacts and hole-dominant behaviour with In/Pd contacts. The length and width of the In/Au-contacted device are 1 μm and 2 μm and of the In/Pd device are 0.5 μm and 1 μm. The inset provides the energy band levels of WSe_2 and the metal where E_C and E_V refer to the conduction and valence band energies, respectively, of the 2D semiconductor. **c**, Linear output characteristics of the device. **d**, **e**, Comparison of contact resistance and drain current with values reported in the literature[9,27–33].

Typical transfer and output curves for In/Au-contacted monolayer MoS_2 as the channel in FETs are shown in Fig. 2d, e. The devices were fabricated on off-the-shelf thermal SiO_2 (300 nm) on Si substrates and were not encapsulated. Despite this, the transfer characteristics such as those shown in Fig. 2d exhibited sharp turn on and high currents with mobility values reaching $167 \pm 20\ cm^2\ V^{-1}\ s^{-1}$. Measurements of mobility with temperature reveals that the phonon-limited mobility scales as $\mu \propto T^{-1}$ at low temperatures and as $\mu \propto T^{-1.6}$ at high temperatures because of acoustic phonon scattering[20] (Extended Data Fig. 2f). The FETs also exhibit linear output characteristics both at room temperature and at low temperatures (Extended Data Fig. 2d, e), suggesting the absence of a Schottky barrier. The highest current density we obtained for multi-layered MoS_2 FETs was 196 $\mu A\ \mu m^{-1}$ (see Extended Data Table 1 for comparison with literature). Measurements as a function of temperature reveal the Schottky barrier height to be around 110 meV (Extended Data Fig. 2g, h), which is consistent with the work function of the metal and the conduction-band energy level of MoS_2.

In addition to MoS_2, we have also deposited In/Au on other 2D transition-metal dichalcogenides such as NbS_2, WS_2 and WSe_2. It can be seen from Fig. 3a that we obtain a contact resistance of 220 $\Omega\ \mu m$ for NbS_2 grown by CVD, which is among the lowest values reported for any metal contact on a 2D transition-metal dichalcogenide. The TLM plot in Fig. 3b shows that the contact resistance for WS_2 is $2.4 \pm 0.5\ k\Omega\ \mu m$, which is also among the lowest reported in the literature, as indicated by the summary of results shown in Fig. 3c. The low contact resistance in WS_2 translates into better FET performance, as indicated by the transfer characteristics shown in Fig. 3d where substantially higher mobility ($83 \pm 10\ cm^2\ V^{-1}\ s^{-1}$) can be observed for In/Au contacts in comparison with titanium electrodes ($1.2 \pm 1\ cm^2\ V^{-1}\ s^{-1}$). Output curves of WS_2 devices are given in Extended Data Fig. 3.

We have also confirmed the formation of an ultraclean interface on WSe_2. The cross-sectional ADF STEM image of In/Au electrodes on two layers of WSe_2 shown in Fig. 4a reveals a clean van der Waals interface with spacing of 2.94 Å between the metal and Se, as indicated in the schematic. In/Au alloy electrodes on WSe_2 yield ambipolar FET characteristics with the electron current being higher than the hole current, as shown in Fig. 4b. The output results for both p-type and n-type devices are provided in Fig. 4c. The resistance for electron injection is 16 $k\Omega\ \mu m$ and for holes it is 225 $k\Omega\ \mu m$. These large values are consistent with the large energy offsets between the Fermi level of In (4.10 eV), the conduction (3.50 eV) and valence (4.83 eV) bands of WSe_2 (see inset of Fig. 4b). Our measurements reveal that the energy barrier for hole injection is 0.73 eV and the energy barrier for electrons is 0.60 eV. Therefore, we expect the hole current to be less than the electron current with In/Au electrodes, which is consistent with our measurements. The energy barriers for carrier injection into WSe_2 match ideally with the band offsets and the FET properties. This also suggests that the In alloy contacts form clean interfaces with WSe_2 without the creation of defects or local reactions. A comparison of contact resistance and drain current values (shown in Fig. 4d, e) reveals that the In/Au contacts yield the lowest contact resistance and that both the electron and hole currents are higher than values in the literature.

Finally, the soft nature of In allows it to form stable alloys readily with other metals (Extended Data Figs. 4 and 5). This property can be used to adjust the work function of electrodes to facilitate electron or hole injection while maintaining the ultraclean interface. To demonstrate this, we deposited 3 nm of In and 100 nm of the high-work-function metal Pd on top. The Kelvin force microscopy results shown in Extended Data Fig. 6 show that the work function of the alloy is slightly increased, as indicated in the inset of Fig. 4b. The typical transfer curves of FET devices with In/Pd alloy electrodes given in Fig. 4b exhibit higher hole current and lower electron current owing to the increased work function. The measurements indicate that the energy barrier for hole injection is 0.63 eV and the energy barrier for electrons is 0.7 eV. The free adjusted barrier height indicates a clean interface between the WSe_2 and the In alloy without Fermi-level pinning.

In summary, our results demonstrate ultraclean van der Waals contacts on a variety of truly 2D semiconductors. The resulting devices from such clean contacts exhibit excellent performance. Our results should lead to the realization of ultrathin electronics based on 2D semiconductors.

Online content

Any methods, additional references, Nature Research reporting summaries, source data, statements of data availability and associated accession codes are available at https://doi.org/10.1038/s41586-019-1052-3.

Received: 24 September 2018; Accepted: 22 January 2019;
Published online 27 March 2019.

1. Chhowalla, M., Jena, D. & Zhang, H. Two-dimensional semiconductors for transistors. *Nat. Rev. Mater.* **1**, 16052 (2016).
2. Jena, D., Banerjee, K. & Xing, G. H. 2D crystal semiconductors: intimate contacts. *Nat. Mater.* **13**, 1076–1078 (2014).
3. Allain, A., Kang, J., Banerjee, K. & Kis, A. Electrical contacts to two-dimensional semiconductors. *Nat. Mater.* **14**, 1195–1205 (2015).
4. Radisavljevic, B., Radenovic, A., Brivio, J., Giacometti, V. & Kis, A. Single-layer MoS_2 transistors. *Nat. Nanotechnol.* **6**, 147–150 (2011).
5. Das, S., Chen, H.-Y., Penumatcha, A. V. & Appenzeller, J. High performance multilayer MoS_2 transistors with scandium contacts. *Nano Lett.* **13**, 100–105 (2013).
6. Guimarães, M. H. D. et al. Atomically thin ohmic edge contacts between two-dimensional materials. *ACS Nano* **10**, 6392–6399 (2016).
7. Yu, L. et al. Graphene/MoS_2 hybrid technology for large-scale two-dimensional electronics. *Nano Lett.* **14**, 3055–3063 (2014).
8. Park, W. et al. Complementary unipolar WS_2 field-effect transistors using Fermi-level depinning layers. *Adv. Electron. Mater.* **2**, 1500278 (2016).
9. Yamamoto, M., Nakaharai, S., Ueno, K. & Tsukagoshi, K. Self-limiting oxides on WSe_2 as controlled surface acceptors and low-resistance hole contacts. *Nano Lett.* **16**, 2720–2727 (2016).
10. Liu, Y. et al. Toward barrier free contact to molybdenum disulfide using graphene electrodes. *Nano Lett.* **15**, 3030–3034 (2015).
11. Chee, S.-S. et al. Lowering the Schottky barrier height by graphene/Ag electrodes for high-mobility MoS_2 field-effect transistors. *Adv. Mater.* **31**, 1804422 (2019).
12. Liu, Y. et al. Approaching the Schottky–Mott limit in van der Waals metal–semiconductor junctions. *Nature* **557**, 696–700 (2018).
13. Desai, S. B. et al. MoS_2 transistors with 1-nanometer gate lengths. *Science* **354**, 99–102 (2016).
14. Kappera, R. et al. Phase-engineered low-resistance contacts for ultrathin MoS_2 transistors. *Nat. Mater.* **13**, 1128–1134 (2014).
15. Cui, X. et al. Low-temperature ohmic contact to monolayer MoS_2 by van der Waals bonded Co/h-BN electrodes. *Nano Lett.* **17**, 4781–4786 (2017).
16. Kim, C. et al. Fermi level pinning at electrical metal contacts of monolayer molybdenum dichalcogenides. *ACS Nano* **11**, 1588–1596 (2017).
17. English, C. D. et al. Improved contacts to MoS_2 transistors by ultra-high vacuum metal deposition. *Nano Lett.* **16**, 3824–3830 (2016).
18. Smithe, K. K. H. et al. Intrinsic electrical transport and performance projections of synthetic monolayer MoS_2 devices. *2D Mater.* **4**, 011009 (2016).
19. Kondekar, N. P. et al. In situ XPS investigation of transformations at crystallographically oriented MoS_2 interfaces. *ACS Appl. Mater. Interfaces* **9**, 32394–32404 (2017).
20. Yu, Z. et al. Analyzing the carrier mobility in transition-metal dichalcogenide MoS_2 field-effect transistors. *Adv. Funct. Mater.* **27**, 1604093 (2017).
21. Gao, J. et al. Transition-metal substitution doping in synthetic atomically thin semiconductors. *Adv. Mater.* **28**, 9735–9743 (2016).
22. Liu, H. et al. Statistical study of deep submicron dual-gated field-effect transistors on monolayer chemical vapor deposition molybdenum disulfide films. *Nano Lett.* **13**, 2640–2646 (2013).
23. Smithe, K. K. H. et al. Low variability in synthetic monolayer MoS_2 devices. *ACS Nano* **11**, 8456–8463 (2017).
24. Iqbal, M. W. et al. Tailoring the electrical and photo-electrical properties of a WS_2 field effect transistor by selective n-type chemical doping. *RSC Adv.* **6**, 24675–24682 (2016).
25. Khalil, H. M. W. et al. Highly stable and tunable chemical doping of multilayer WS_2 field effect transistor: reduction in contact resistance. *ACS Appl. Mater. Interfaces* **7**, 23589–23596 (2015).
26. Kim, Y. J. et al. Contact resistance reduction of WS_2 FETs using high-pressure hydrogen annealing. *IEEE J. Electron Devices Soc.* **6**, 164–168 (2018).
27. Tosun, M. et al. Air-stable n-doping of WSe_2 by anion vacancy formation with mild plasma treatment. *ACS Nano* **10**, 6853–6860 (2016).
28. Movva, H. C. P. et al. High-mobility holes in dual-gated WSe_2 field-effect transistors. *ACS Nano* **9**, 10402–10410 (2015).
29. Wang, J. I.-J. et al. Electronic transport of encapsulated graphene and WSe_2 devices fabricated by pick-up of prepatterned hBN. *Nano Lett.* **15**, 1898–1903 (2015).
30. Das, S. & Appenzeller, J. WSe_2 field effect transistors with enhanced ambipolar characteristics. *Appl. Phys. Lett.* **103**, 103501 (2013).
31. Fang, H. et al. Degenerate n-doping of few-layer transition metal dichalcogenides by potassium. *Nano Lett.* **13**, 1991–1995 (2013).

32. Chuang, H.-J. et al. High mobility WSe_2 p- and n-type field-effect transistors contacted by highly doped graphene for low-resistance contacts. *Nano Lett.* **14**, 3594–3601 (2014).
33. Zhou, C. et al. Carrier type control of WSe_2 field-effect transistors by thickness modulation and MoO_3 layer doping. *Adv. Funct. Mater.* **26**, 4223–4230 (2016).

Acknowledgements M.C., Y.W. and J.Y. acknowledge support from the US National Science Foundation (Civil, Mechanical and Manufacturing Innovation 1727531, Electrical Communications and Cyber Systems 1608389) and Air Force Office of Scientific Research Award FA9550-16-1-0289. M.C. and X.S. acknowledge support from the Shenzhen Peacock Plan (grant number KQTD2016053112042971). J.M. acknowledges support from the Rutgers RiSE summer internship programme. H.Y.J. acknowledges support from the Creative Materials Discovery Program through the National Research Foundation of Korea (NRF-2016M3D1A1900035). R.J.W. and A.M. acknowledge partial support from US NSF MRSEC Award DMR-1420013 for Characterization Facility at the University of Minnesota.

Author contributions M.C. conceived the idea, supervised the project and wrote the paper. Y.W. prepared and measured all devices. J.C.K. and H.Y.J. performed sample fabrication using focused ion beam and STEM on monolayer MoS_2, NbS_2 and WSe_2. R.J.W. and A.M. performed STEM on few-layered MoS_2. J.M. assisted in making contacts and measured work functions. X.S. synthesized 2D materials by CVD. J.Y. performed XPS and analysed data. F.Z. assisted in device fabrication and In deposition. All authors read the paper and agreed on its content.

Competing interests The authors declare no competing interests.

Additional information
Extended data is available for this paper at https://doi.org/10.1038/s41586-019-1052-3.
Supplementary information is available for this paper at https://doi.org/10.1038/s41586-019-1052-3.
Reprints and permissions information is available at http://www.nature.com/reprints.
Correspondence and requests for materials should be addressed to M.C.
Publisher's note: Springer Nature remains neutral with regard to jurisdictional claims in published maps and institutional affiliations.

METHODS

Sample preparation and device fabrication. Monolayer MoS_2 was grown by CVD using MoO_3 and sulfur powder as precursors. 100 mg of MoO_3 and 400 mg of sulfur were placed in two small tubes in the upstream of the tube furnace. A small drop of perylene-3,4,9,10-tetracarboxylic acid tetrapotassium salt (PTAS) was dropped on SiO_2/Si substrates as a seed to trigger growth of monolayer MoS_2. The substrates were placed face-up on top of an alumina boat in the centre of the furnace. Air was evacuated by flowing argon (Ar, ultrahigh purity, Air Gas) for 15 min at 200 standard cubic centimeters per minute (sccm). The tube was heated at 200 °C for 15 min to remove moisture from the precursors. Then the temperature was increased to 870 °C under a 90 sccm Ar flow and the MoO_3 and S source were heated to 250 °C and 170 °C, respectively. After 20 min, the furnace was cooled down to room temperature and the samples were removed from the furnace.

Few-layered transition-metal dichalcogenides were prepared by mechanically exfoliating flakes from the bulk crystals (MoS_2, WS_2 and WSe_2, purchased from HQ Graphene) via the Scotch tape method. Thermally grown 300-nm-thick SiO_2 substrates on heavily doped Si were used as the gate insulator and electrode, respectively. Monolayer or multilayer flakes were identified with optical microscopy and atomic force microscopy. Then electron-beam lithography was used to pattern the electrodes. Before metal electrode deposition, the evaporation system was pumped to a base pressure of $<10^{-6}$ Torr. Then, 10-nm-thick In was deposited with a low rate of 0.2 Å s^{-1} and 100-nm-thick Au was deposited subsequently. The device was rinsed with isopropanol after immersing in acetone for lift-off. Once the fabrication process was completed, all devices were annealed at 200 °C in H_2/Ar gas for one hour before measurements.

Measurements. Transport characteristics were measured by applying voltage with the Keithley 4200 semiconductor parameter analyser system. The low-temperature measurements were performed in a vacuum probe station with liquid nitrogen and a temperature controller. XPS was performed using the Thermo Scientific K-Alpha system. Atomic force microscopy and scanning Kelvin probe microscopy were performed using the Park NX-Hivac system. Photoluminescence data were collected using a 532-nm laser excitation focused through a ×100 objective lens. The spectra were taken at an incident laser power of 50 μW, which was sufficiently low to avoid any damage to the sample.

Schottky barrier extraction. The Schottky barrier height of the contact was extracted by measuring the activation energy in the thermionic emission region. In a Schottky-barrier FET, the reverse-biased contact consumes most of the voltage drop and dominates the transistor behaviour. The current density of thermal emission through a metal–semiconductor contact is:

$$J = A^{*} T^{\alpha} \exp\left[-\frac{q\Phi_{\mathrm{B}}}{k_{\mathrm{B}}T}\right]\left[1-\exp\left(-\frac{qV}{k_{\mathrm{B}}T}\right)\right] \quad (1)$$

where $A*$ is the Richardson constant, V is the applied voltage, T is the temperature, α is an exponent equal to 2 for bulk semiconductors and to 3/2 for 2D semiconductors, and k_B is Boltzmann's constant. Using this equation, the slope of the Richardson plot, $\ln(I/T^{3/2}) \approx 1/T$, yields Φ_B as a function of gate voltage. The gate voltage at which the Schottky barrier height tends to curve away from the linear dependence is where the flat band condition occurs because after the gate voltage reaches this condition, carriers are transferred through tunnelling as well. To extract Schottky barrier height, we identify the voltage at which Φ_B stops linearly depending on V_g. As shown in Extended Data Fig. 2f, the Schottky barrier of In/MoS_2 is 110 meV.

STEM specimen preparation and acquisition parameters. Cross-sectional STEM lamellas of the FET samples were prepared using a FEI Helios NanoLab G4 focused ion beam. The cross-sectional STEM images of a monolayer MoS_2 were taken at 200 keV using a FEI Titan^3 G2 60-300 with a double-sided spherical aberration corrector. The probe convergence semi-angle was set to be approximately 25 mrad. ADF STEM images were acquired over the range 50–200 mrad. All electron energy loss spectroscopy measurements were collected in dual mode to enable simultaneous collection of zero-loss and core-loss spectra to compensate for energy drift during specimen acquisition. It is worth noting that the energy drift was tested by continuous collection of zero-loss spectra for 5 min to ensure a reasonable energy drift (<0.3 eV) before beginning any data acquisition.

Data availability

The data that support the findings of this study are available from the corresponding author upon reasonable request.

34. Young, P. A. Lattice parameter measurements on molybdenum disulphide. *J. Phys. Appl. Phys.* **1**, 936 (1968).
35. Sanz, C., Guillén, C. & Herrero, J. Annealing of indium sulfide thin films prepared at low temperature by modulated flux deposition. *Semicond. Sci. Technol.* **28**, 015004 (2013).
36. Kaushik, N. et al. Schottky barrier heights for Au and Pd contacts to MoS_2. *Appl. Phys. Lett.* **105**, 113505 (2014).
37. Du, Y. et al. MoS_2 field-effect transistors with graphene/metal heterocontacts. *IEEE Electron Device Lett.* **35**, 599–601 (2014).
38. Xie, L. et al. Graphene-contacted ultrashort channel monolayer MoS_2 transistors. *Adv. Mater.* **29**, 1702522 (2017).
39. Cui, X. et al. Multi-terminal transport measurements of MoS_2 using a van der Waals heterostructure device platform. *Nat. Nanotechnol.* **10**, 534–540 (2015).
40. Kaushik, N. et al. Interfacial n-doping using an ultrathin TiO_2 layer for contact resistance reduction in MoS_2. *ACS Appl. Mater. Interfaces* **8**, 256–263 (2016).
41. Wang, J. et al. High mobility MoS_2 transistor with low Schottky barrier contact by using atomic thick h-BN as a tunneling layer. *Adv. Mater.* **28**, 8302–8308 (2016).
42. Yin, X. et al. Tunable inverted gap in monolayer quasi-metallic MoS_2 induced by strong charge-lattice coupling. *Nat. Commun.* **8**, 486 (2017).
43. Kim, H.-J. et al. Enhanced electrical and optical properties of single-layered MoS_2 by incorporation of aluminum. *Nano Res.* **11**, 731–740 (2018).
44. Park, W. et al. Contact resistance reduction using Fermi level de-pinning layer for MoS_2 FETs. In *IEEE International Electron Devices Meeting* 5.1.1–5.1.4, https://ieeexplore.ieee.org/abstract/document/7046986 (IEEE, 2014).
45. Cho, K. et al. Contact-engineered electrical properties of MoS_2 field-effect transistors via selectively deposited thiol-molecules. *Adv. Mater.* **30**, 1705540 (2018).
46. Yang, L. et al. Chloride molecular doping technique on 2D materials: WS_2 and MoS_2. *Nano Lett.* **14**, 6275–6280 (2014).
47. Kang, J., Liu, W. & Banerjee, K. High-performance MoS_2 transistors with low-resistance molybdenum contacts. *Appl. Phys. Lett.* **104**, 093106 (2014).
48. Cheng, Z. et al. Immunity to scaling in MoS_2 transistors using edge contacts. Preprint at https://arxiv.org/abs/1807.08296 (2018).

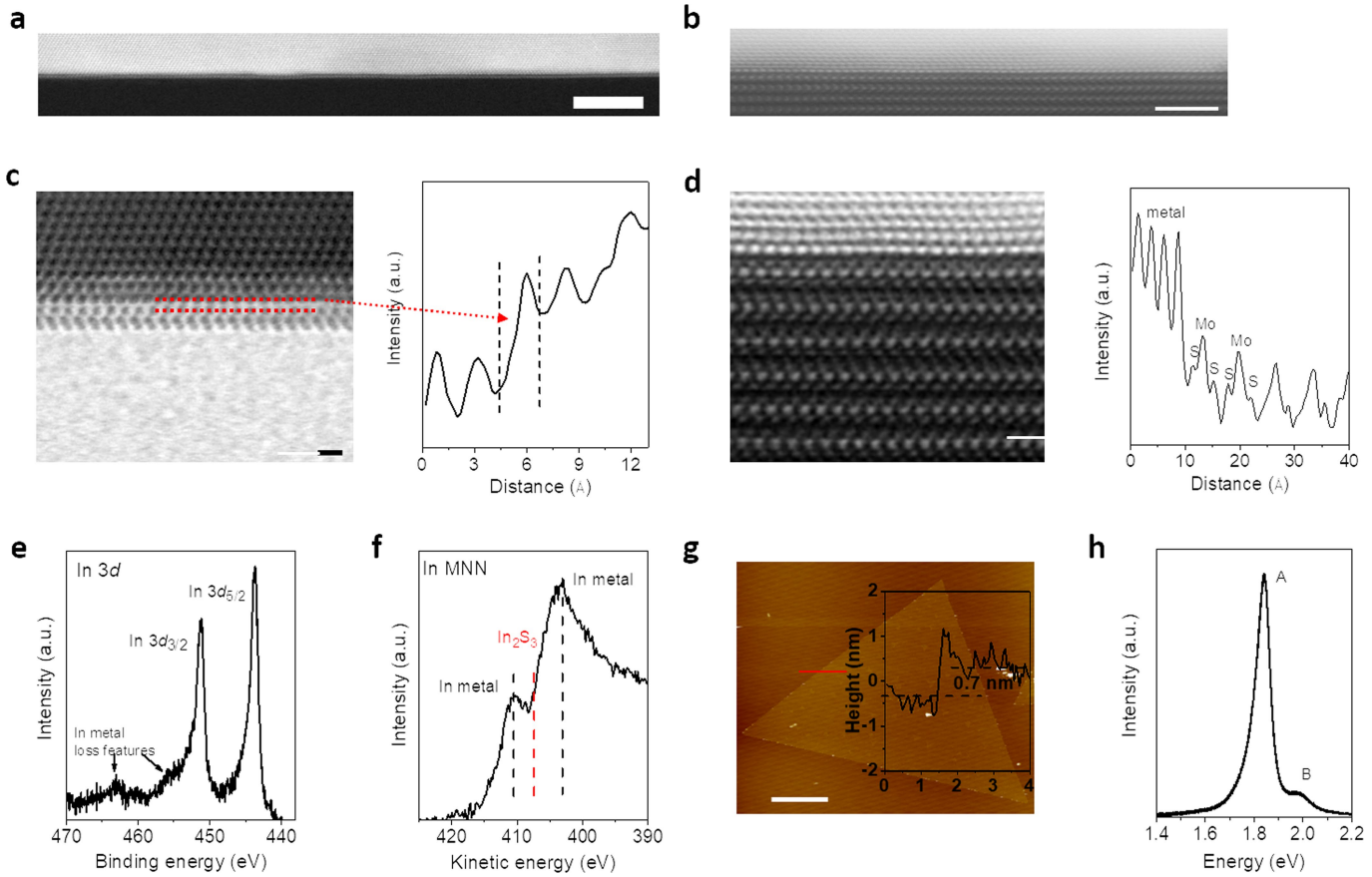

Extended Data Figure 1 | Atomic resolution imaging and chemical analyses of the In/Au–MoS_2 interface. a, Broader view STEM images of three-dimensional metal on 2D semiconductor. Cross-sectional STEM image of interface between In/Au and monolayer MoS_2. Scale bar, 5 nm. **b**, Cross-sectional STEM image of interface between In/Au and multi-layered MoS_2. Scale bar, 2 nm. **c**, Bright-field STEM of In/Au contact to monolayer MoS_2. The intensity profile shows that the distance between the In/Au atoms of the electrode metal to sulfur atoms in the first layer is 2.4 Å. **d**, ADF-STEM and intensity profile of In/Au contact to multilayer MoS_2. The intensity profile shows that the MoS_2 interlayer distance is 6.2 Å, which is consistent with the literature[34]. The distance between the sulfur atoms in adjacent layers is 2.7 Å and the distance between the In/Au atoms and sulfur atoms in the first layer is also 2.7 Å for multi-layered samples, indicating a van der Waals contact at the interface. **e**, XPS image of the In/Au–MoS_2 interface showing In metal $3d_{5/2}$ (443.8 eV) and $3d_{3/2}$ (451.4 eV) peaks along with In metal loss features. **f**, X-ray-induced Auger spectrum showing a pristine In metal peak at 402.9 eV. In_2O_3 has a clear peak at 400.2 eV, which is absent in our samples. There is no sign of In_2S_3 (407.3 eV) and In MNN Auger spectra indicate no chemical reaction at the interface[35]. **g**, Atomic force microscopy image of CVD-grown monolayer MoS_2. **h**, Photoluminescence of CVD-grown MoS_2, with the A exciton peak at 1.84 eV and the B exciton peak at 1.97 eV clearly visible.

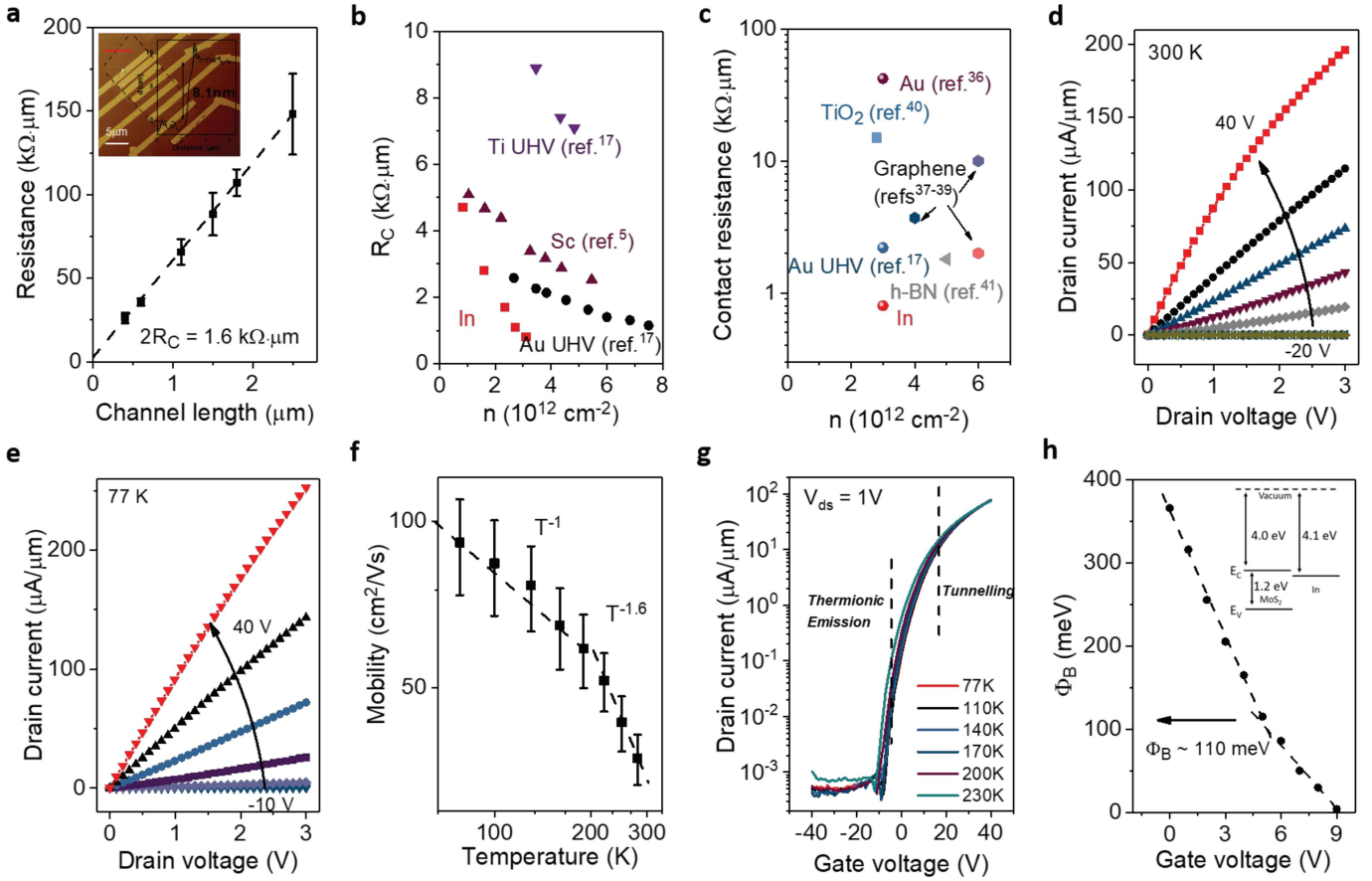

Extended Data Figure 2 | Contact resistance and device properties of In/Au electrodes on few-layered MoS_2. a, TLM results of In/Au contacts on few-layered MoS_2. **b**, Contact resistance R_C versus carrier concentration for In/Au electrodes. Sc, Ti and Au electrodes deposited under ultrahigh vacuum (UHV, 10^{-9} Torr) are provided for comparison[5,17]. **c**, Comparison of contact resistance from the literature and our results for different types of electrode materials[17,36–41]. **d**, Typical output curve at room temperature shows that the highest current density is 196 μA μm^{-1}. **e**, Output characteristics at low temperature, with the linearity of the output characteristics indicating the absence of a contact barrier. **f**, Mobility versus temperature reveals phonon-limited mobility at low temperature and acoustic phonon scattering at high temperature. **g**, Transfer characteristics with temperature showing the metal–insulator transition. **h**, Schottky barrier (Φ_B) extraction indicating ideal In contacts with MoS_2. The inset shows the energy band diagram of MoS_2 and In.

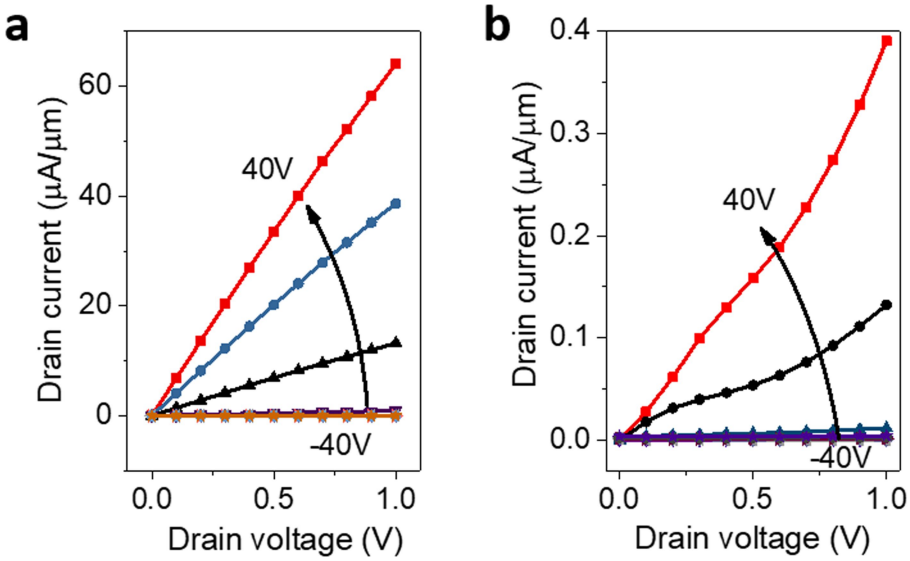

Extended Data Figure 3 | Output characteristics of WS_2. a, In contacts. **b**, Ti contacts.

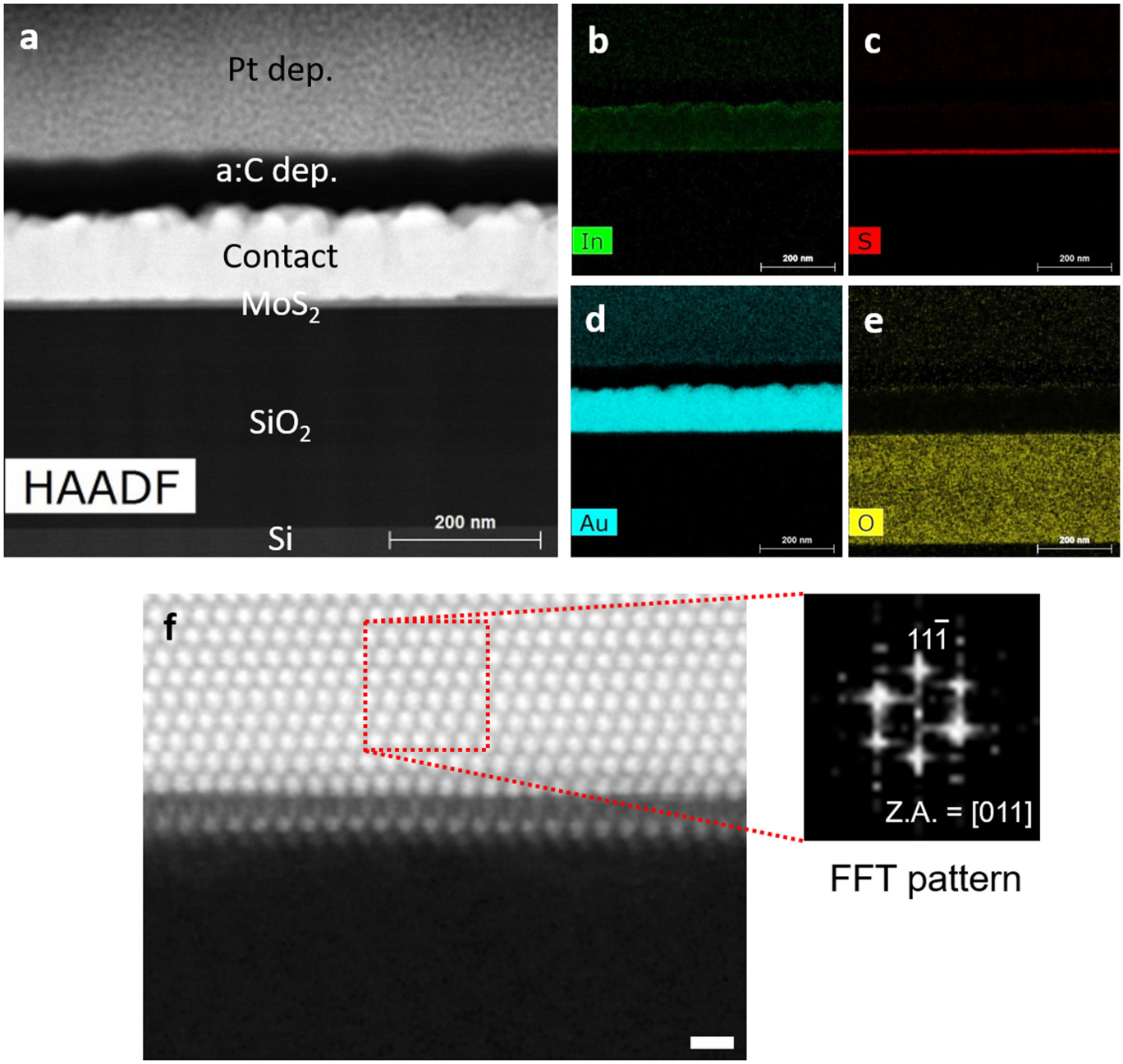

Extended Data Figure 4 | Energy-dispersive X-ray spectroscopy mapping of the contact. a, Low-magnification cross-sectional high-angle annular dark-field (HAADF) STEM image of the MoS_2 with In/Au contact. **b**–**e**, Elemental mapping showing the distribution of In, Au, S and O. In and Au overlap over the entire metal layer, suggesting the formation of an alloy. S is observed underneath the In and Au. O is obtained primarily from SiO_2 of the substrate. **f**, Fast Fourier transform (FFT) pattern from metal electrode showing alloying between In and Au. Scale bar, 5 Å. The diffraction pattern is of a face-centred cubic alloy. Pure In has body-centred cubic crystal structure. a:C, amorphous carbon; dep., deposition; Z.A., zone axis.

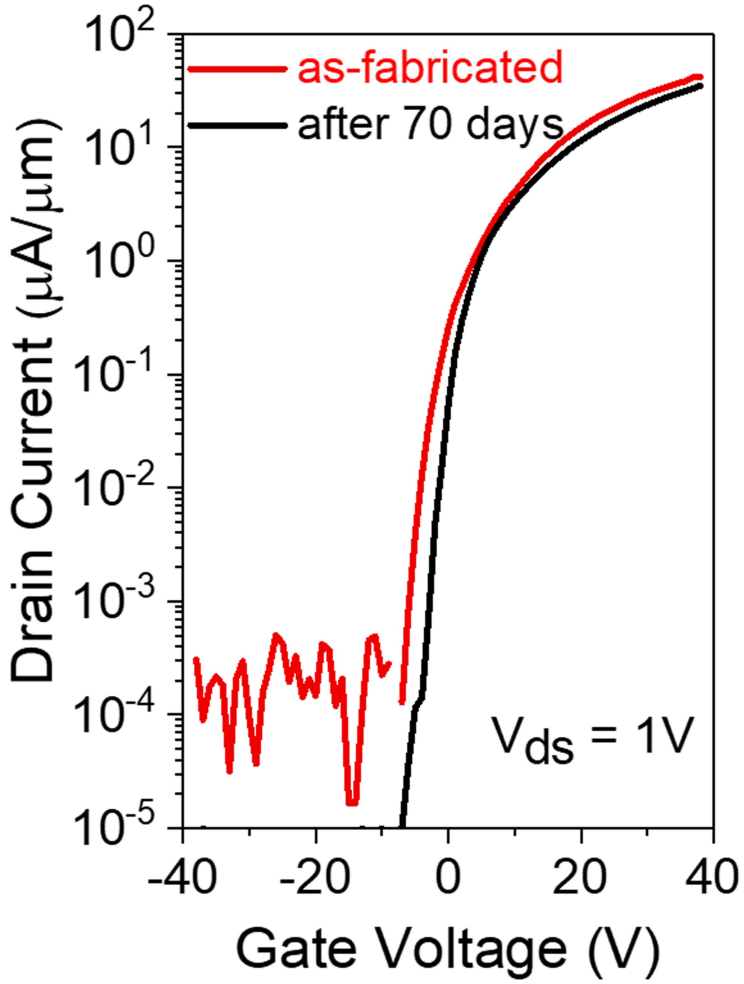

Extended Data Figure 5 | Typical transfer characteristics of the device measured immediately after fabrication and after 70 days.

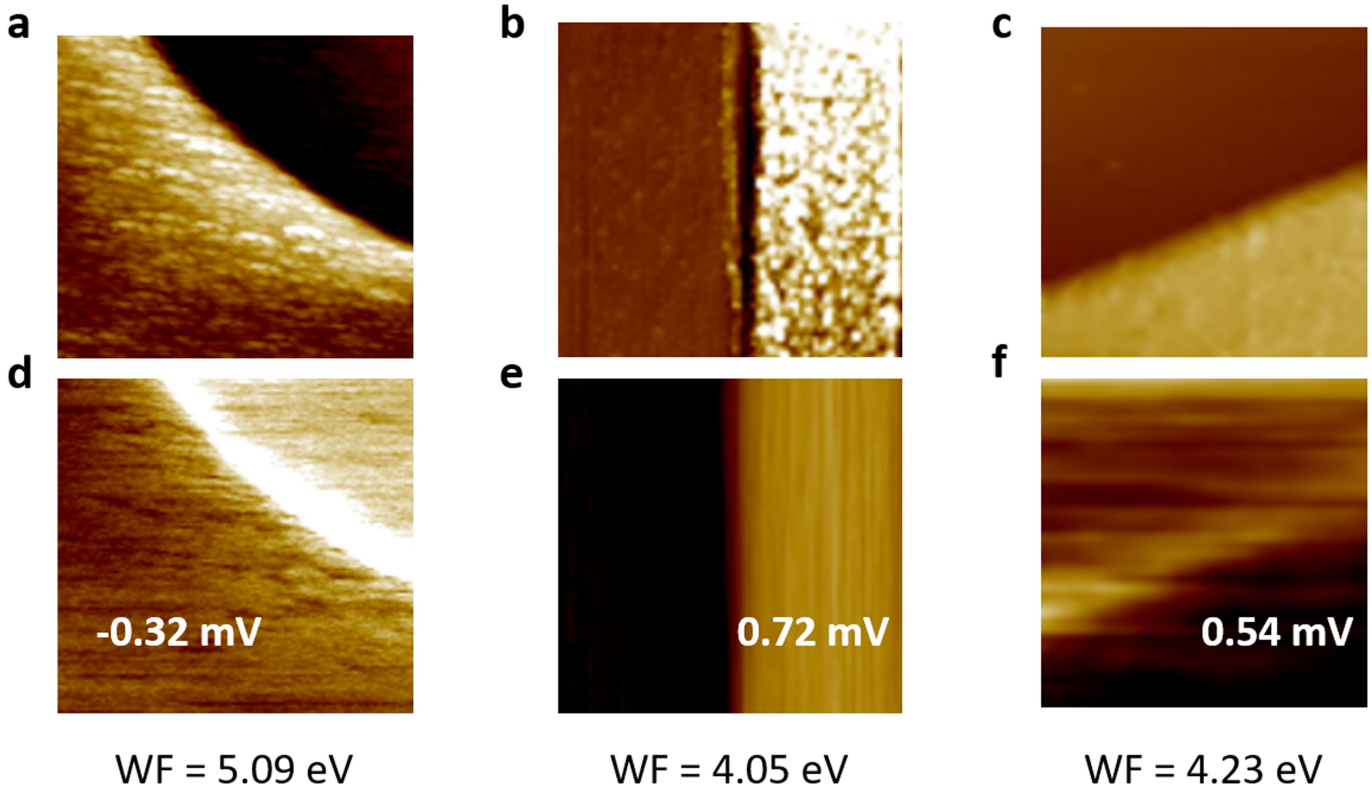

Extended Data Figure 6 | Topographical and scanning Kelvin probe microscopy images. a, **d**, Topographical and surface potential results of the Au sample; the work function (WF) extracted is 5.09 eV, similar to the theoretical value. **b**, **e**, Topographical and surface potential results of the In/Au sample; the work function extracted is very close to that of the In work function, 4.05 eV. **c**, **f**, Topographical and surface potential results of the In/Pd sample; the work function extracted is 4.23 eV, higher than that of In/Au.

Extended Data Table 1 | Literature survey of device performance

Method	Channel length (μm)	EOT	Gate voltage (V)	Drain voltage (V)	I_{ON} (μA/μm)	R_C (kΩ·μm)	ref
	Monolayer MoS_2						
In/Au clean contact	2	300 nm SiO_2	40	1	18	3	This work
Graphene	5	285 nm SiO_2	80	0.1	0.8	NA	10
Graphene edge contact	7	30 nm HfO_2	3	0.025	0.1	59	6
Graphene/Ag	4	300 nm SiO_2	80	1	5	115	11
Co/h-BN	0.2	BN+285 nm SiO_2	80	0.01	0.1	6	15
Au UHV	1.2	90 nm SiO_2	35	1	12	5	18
Cr contact	1	285 nm SiO_2	40	1	4	40	16
Re doping	10.5	300 nm SiO_2	80	0.1	0.05	26.25	21
Double gate	0.1	B: 285 nm SiO_2 T: 16 nm $Al2O_3$	40	1	12	10	22
Ag/Au	4	30 nm SiO_2	25	1	17	12	23
1T'/Au	10	285 nm SiO_2	50	1	1.8	NA	42
Al_2O_3 passivation	1.5	300 nm SiO_2	100	1	0.5	NA	43
	Multilayer MoS_2						
In/Au clean contact	0.5	300 nm SiO_2	40	3	196	0.8	This work
Sc	5	15 nm Al_2O_3	8	3	160	NA	5
Graphene contact	5	285 nm SiO_2	60	0.1	1	NA	10
Transferred Ag	0.16	BN+90 nm SiO_2	40	3	660	NA	12
Phase engineering	1.2	300 nm SiO_2	30	5	85	0.24	14
Au UHV	0.5	90 nm SiO_2	25	1	75	2	17
Graphene edge contact, h-BN	5	285 nm SiO_2	80	0.05	0.2	2.5	39
h-BN tunneling	0.3	255 nm SiO_2	40	1	30	4	41
Fermi level de-pinning	1.5	90 nm SiO_2	20	3	24	5.4	44
Molecules doping	2	300 nm SiO_2	40	3	50	25.2	45
Cl doping	0.5	90 nm SiO_2	50	1.2	200	0.5 (2×10^{13} cm^{-2})	46
K doping	0.5	B: 285 nm SiO_2 T: 17.5 nm ZrO_2	40 1.5	2.5	15	NA	31
Mo	2	72 nm Al_2O_3	30	3	140	2 (4×10^{13} cm^{-2})	47
Edge contact	2.2	300 nm SiO_2	30	0.48	0.8	205	48

Contact resistances are extracted at a carrier concentration of around 3×10^{12} cm^{-2} for multilayer MoS_2 and 5×10^{12} cm^{-2} for monolayer MoS_2 except where indicated otherwise. EOT, equivalent oxide thickness. I_{ON} is the drain current when the device is in the 'ON' state. 1T' represents distorted octahedral structure. Missing values are represented by NA (not available). Data are from refs [5,6,10–12,14–18,21–23,31,39,41–48].